Dynamics of Hydrogen–Ammonia–Natural Gas Lean-Premixed High-Pressure Flames

Tristan T. Shahin[a,*], Alexander J. Hodge[a], Benjamin K. Murdock[b], Thomas N. McLean[a], Keaton C. Koenig[a], Rohan M. Gejji[a], Robert P. Lucht[a,b], Carson D. Slabaugh[a]

[a] *School of Aeronautics & Astronautics, Purdue University, West Lafayette, IN 47907, United States*
[b] *School of Mechanical Engineering, Purdue University, West Lafayette, IN 47907, United States*

Abstract

The influence of fuel composition on self-excited combustion instabilities in a high-pressure combustor operated with ammonia, hydrogen, and natural gas fuels is characterized with high-frequency pressure measurements and imaging of the flame structure. A micromix multi-stage injector with 19 elements is used to introduce the fuel blend premixed with heated air into an optically accessible combustor operated at ∼1.1 MPa. As hydrogen is substituted for natural gas, longitudinal thermoacoustic instabilities are observed in the combustor with pressure fluctuation amplitudes as large as 8% of the mean chamber value. In the absence of natural gas, limit-cycle instability magnitude is largely insensitive to ammonia addition. However, fuel compositions with $> 20\%$ natural gas result in positive correlation between instability amplitude and ammonia concentration. Spatial distribution of heat release in the combustor evaluated from OH* chemiluminescence imag-

*Corresponding author
Email address: tshahin@purdue.edu (Tristan T. Shahin)

ing reveals axial growth in the regions of heat release fluctuation as hydrogen decreases, thus correlating flame length to instability amplitude. Distinct transitions from the first harmonic of the fundamental longitudinal acoustic mode ($\sim$1100 Hz) to the fundamental mode ($\sim$550 Hz) are observed with root mean square pressure fluctuations exceeding 7% of the mean chamber value. These cases correspond to hydrogen mole fractions $\leq$ 50%. Analysis of the phase relationship between pressure fluctuations upstream and downstream of the flame zone indicates acoustic coupling of the injector as a key contributor to instability growth.

Nomenclature

$1L$	=	half-wave pressure mode shape
$2L$	=	full-wave pressure mode shape
Da	=	Damköhler number, computed from the quotient of τ_{flow} and τ_k
D_{inj}	=	single micromixer element diameter
I'	=	hydroxyl radical (OH^*) chemiluminescence intensity fluctuation
$\dot{m}_{air}$	=	air mass flow rate, kg/s
p_{CC}	=	mean chamber pressure, bar
p_{IN}	=	inlet air pressure, bar
p'_{RMS}	=	root mean square of pressure fluctuation
RI	=	Rayleigh index, computed from the cycle integrated product of p' and I'
T_{AD}	=	computed equillibrium flame temperature, K
T_{IN}	=	inlet air temperature, K
$\bar{U}$	=	average injector center-line velocity
η	=	ammonia decomposition efficiency
τ_k	=	premixed laminar flame kinetic timescale
τ_{flow}	=	convective flow timescale
ϕ	=	equivalence ratio
$\Phi_{p'-I'}$	=	phase difference between p' and I' at x/L = 0.02
$\Phi_{p'-p'}$	=	phase difference between p' at x/L = -0.25 and p' at x/L = 0.25
χ	=	hydrogen fraction
ψ	=	phase angle of SPOD reconstruction

Subscripts

x = axial direction, where $x = 0$ corresponds to the combustor face

y = radial direction, where $y = 0$ corresponds to the combustor centerline

θ = azimuthal direction, where $\theta = 0$ corresponds to the x-y plane

1. Introduction

Decarbonization efforts in chemical power generation necessitate improvements in performance of combustion-based turbines fueled with carbon free energy carriers, and mixtures of these carriers with traditional fuels such as natural gas [1]. Fuel flexible operation of these systems is critical, as discrepancies between fuel availability and demand may occur during this transition. Hydrogen is a widely available fuel candidate with existing pathways for renewable production, but lacks the energy density required for efficient distribution and storage in a gaseous state [2]. Anhydrous ammonia, a carbon free hydrogen carrier, boasts a larger volumetric hydrogen density than liquid hydrogen with preexisting storage and transport infrastructure [3]. Additionally, partial cracking of ammonia through catalytic decomposition can enable in-situ hydrogen formation prior to combustion. This method of co-firing ammonia with hydrogen has been shown to increase combustion performance compared to flames with pure ammonia [4]. A heat recovery system within the turbine exhaust flow can provide the latent enthalpy required to vaporize the ammonia, enhancing the rates of mixing and ignition compared to direct liquid injection [5, 6].

Despite these benefits, the disparate chemical and physical timescales of hydrogen, natural gas, and ammonia introduce significant challenges to the efficiency of combustion devices. Previous efforts to characterize the operabil-

ity of ammonia, hydrogen, and methane blends in traditional lean-premixed swirl combustors observed narrow limits bounded by blow-out at high ammonia concentrations and flashback at high hydrogen concentrations [7, 8]. The required changes in injector design to facilitate combustor operation across this operating space result in a deficit of available information with all three fuels, especially at elevated pressures.

Understanding of combustor operability concerns such as flashback and lean blowout is crucial to realizing the potential benefits of decarbonized fuels. This issue is of principal concern for combustors operating with hydrogen, where high flame speeds increase the likelihood of flashback. Velocity gradients in the reactant boundary layer can provide sufficient conditions for flame propagation upstream into the injector [9]. Flashback propensity is also sensitive to flame-surface interaction. A low temperature wall can extract a sufficiently large amount of heat from the flame to quench it, but this convective and radiative heat transfer can also raise the wall temperature enough to reduce heat flux and prevent quenching [10]. Additionally, the physical processes by which turbulent flame speed varies in premixed turbulent flames with significant hydrogen concentration is not well understood [11]. The combined effect of these complex physical processes leads to particular difficulty in prediction of combustor operability with hydrogen.

Lean premixed gas turbine combustion systems operate very close to the lean blowout limit and are highly susceptible to acoustic disturbances [12–15]. The effect of hydrogen addition on combustion dynamics has been a research area of particular interest in recent years [16–23]. Lim et al. [16] observed a reduced phase lag between velocity perturbations and flame re-

sponse by adding hydrogen to a premixed methane-air flame. They attribute this result to a reduced mean flame length, which lowers the convective time over which heat release occurs. Along with changes in axial flame length, variations in hydrogen concentration can produce geometric effects such as wall interactions that result in nonlinear acoustic coupling, requiring flame describing functions to characterize [24, 25]. Æsøy et al. [17] observed an increase in coherent reactant burning with hydrogen addition, caused by flame tip acceleration, allowing for flame propagation across the reactant jet and into the outer shear layer of a bluff-body stabilized flame. This indicates that increased flame speed and extinction strain rates associated with hydrogen combustion can produce much higher limit-cycle amplitudes in self-excited combustion instabilities. In partially-premixed combustors, hydrogen enrichment has been shown to produce bi-modal thermoacoustic instabilities through a combined effect of local equivalence ratio fluctuations and heat release coupling to vortex shedding from the centerbody tip [21]. Instability behavior can see significant alteration through these complex physical processes, and an additional degree of complexity is introduced when fuel blends include ammonia.

The slow kinetic rates associated with lean-premixed ammonia-air flames limit combustor operability due to increased risk of lean-blowout [7, 8, 26]. At the laboratory scale, experiments with atmospheric ammonia-air flames are often unable to stabilize without air enrichment due to low extinction strain rates [27]. Recent work with counterflow diffusion flames have quantified the extinction limits of ammonia blends with methane and hydrogen [27, 28]. Blends of ammonia and methane are shown to not substantially

increase stability limits for lean blow-out [8, 27]. However, counterflow flame measurements for ammonia-hydrogen fuel blends indicate an order of magnitude increase in extinction strain rate with only 15% hydrogen addition by mole [28]. This result is due to an increase in formation rates for radical species such as H, O, and OH [28, 29]. Increase in extinction strain rate is also correlated to an increase in the blow-out limit in premixed combustors [30]. Increasing pressure can extend the lean blowout limit, but also promotes flashback further limiting the constrained operating space [8].

Recent developments in injector premixing design have led to an increase in dump plane velocity, allowing for stable combustor operation with high hydrogen fuels. The micro-mix injector is one such design, utilizing multi-element premixing tubes that increase injector velocity and result in flame stabilization within the shear layer of each element [31, 32]. Recent work has characterized the flame structure of micromixer flames and the resulting effect on combustion instabilities over a wide range of fuel compositions [18, 33–35]. Kang et al. [18] investigated the effect of hydrogen addition on combustion instabilities in a methane/hydrogen/air flame at atmospheric pressure and observed transition from stable operation with low hydrogen concentration to high amplitude thermoacoustic instabilities at high hydrogen concentration. An observed frequency shift as hydrogen concentration increases is attributed to small-scale vortex roll up and flame surface annihilation that is absent from lower amplitude cases. Jin and Kim [35] investigated the effect of radially staged hydrogen enrichment on combustion instabilities in an ammonia-hydrogen-air flame. They demonstrated a reduction in thermoacoustic coupling with lean-premixed hydrogen-air flames

configured in an annulus around a rich-premixed ammonia-air flame zone when compared to uniform mixtures of the same composition. However, the experiments conducted in these works utilized a shared fuel-air plenum that supplied already premixed reactants to the micromixer. Acoustic isolation of the injection and mixing process in this manner removes the ability to study mechanisms by which combustion dynamics can induce variations in local mixture composition that contribute to heat release fluctuations [21, 36, 37].

The influence of fuel composition on combustion instabilities in a high-pressure technically-premixed combustor operated with ammonia, hydrogen, and natural gas is studied in the current work. A 19-element micro-mixing multi-stage injector is used to introduce ammonia, natural gas, hydrogen, and nitrogen, premixed at varying axial locations with dry, heated air into an optically accessible combustor. As the natural gas and ammonia components of the fuel composition are increased, self-excited longitudinal instabilities are observed in the combustor. Flame structure and dynamics are characterized with an array of high frequency pressure measurements and OH^* chemiluminescence images. The correlation between combustion instability frequency and amplitude to fuel composition and concomitant heat release location is investigated.

2. Experiment Description

2.1. Combustor Hardware

A multi-element premixed combustor operated at a mean chamber pressure (p_{CC}) of ∼10.7 bar with heated unvitiated air, ammonia, natural gas,

hydrogen, and nitrogen was used in the study [38]. A schematic of the experiment is shown in Figure 1. The combustor is made up of three primary sections: an air manifold, an axially staged fuel-air micromixer, and a combustion chamber. Heated air is introduced into the air manifold from a critical-flow sonic nozzle with a computed maximum flowrate uncertainty of 1.2%. The air manifold is isolated from downstream components with 19 choked orifices, connected to each element of the micromixer. The choked inlet condition at the entrance to each micromixer element isolates the air injection process from pressure fluctuations in the combustion chamber. The micromixer is divided into three segments, one each for ammonia, natural gas, and hydrogen injection. The length of the micromixer and the combustion chamber is designed to promote self-excited longitudinal combustion instabilities in the combustor [39–44]. Each fuel injector element is supplied from a manifold with two diametrically opposite orifices with a pressure drop of approximately 20%. The location of fuel injection is set to provide sufficient time for mixing with air to ensure premixed reactants are introduced in the combustion chamber. The fuel injector segments are modular in design and can be interchanged or replaced between tests. As shown in Figure 1, the 19 elements in the micro-mix, multi-stage (M^3) injector are located in a hexagonal grid with equal separation between neighboring elements. The injector flow exits into a 80 mm diameter combustion chamber that is 785 mm long.

A sonic nozzle at the exit of the combustion chamber provides a well-defined acoustic exit boundary condition and pressurizes the combustor. Reactant flows into the external premixer are controlled and metered with

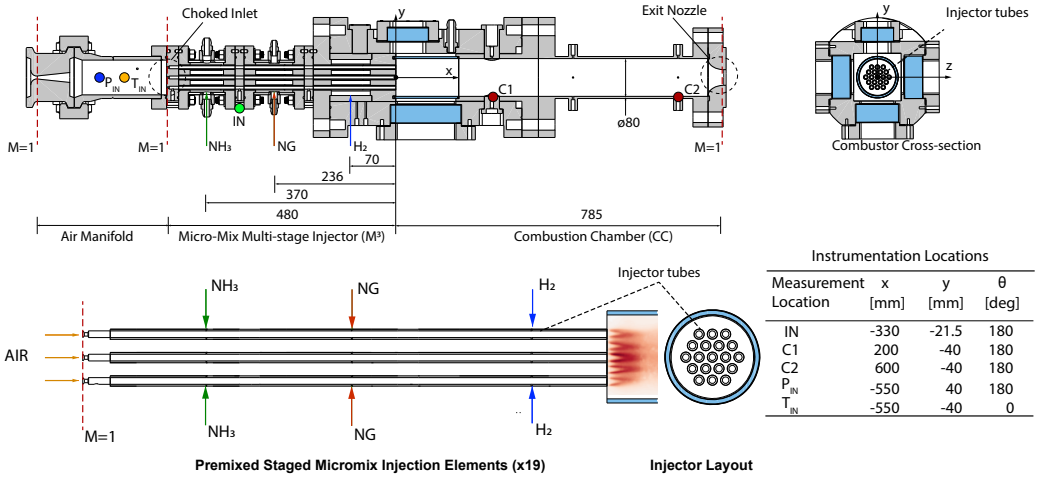

Instrumentation Locations

Measurement Location	x [mm]	y [mm]	θ [deg]
IN	-330	-21.5	180
C1	200	-40	180
C2	600	-40	180
P_{IN}	-550	40	180
T_{IN}	-550	-40	0

Figure 1: Schematic of the combustor with instrumentation probe locations. Pressure instrumentation locations P_{IN}, IN, C1, and C2, and inlet temperature probe location T_{IN} are reported in the table. All dimensions in mm.

critical-flow venturi nozzles that conform to ASME and ISO specifications [45, 46]. The oxidizer used in this study was heated, dry air. Hydrogen was supplied to the experiment from bulk storage at 400 bar [38]. The supplied pipeline natural gas consists of a composition of 92% CH_4, 6% C_2H_6, 0.5% CO_2, 0.3% C_3H_8, and 1.5% N_2 [47]. Liquid anhydrous ammonia is pressurized to target conditions in a piston accumulator assembly. Prior to entering the micromix injector, ammonia is vaporized in a 54 kW electrical heater. Ammonia temperature is measured in the manifold immediately upstream of the injection point. For all test cases, a temperature of 450 ± 30 K is measured, which confirms gas phase ammonia injection. A single injector element is connected to an independently controlled supply of hydrogen and is used as the pilot injector for ignition. Ignition is achieved with a laser-induced spark, delivered at the exit of this pilot element. Once stable ignition is verified, fuel is introduced at target conditions for all injectors and the pilot

hydrogen supply is discontinued. The duration of a typical test is 2 seconds, during which all flow conditions and geometrical parameters are fixed within an equivalence ratio uncertainty less than 2% of the target. This duration is sufficient for the acquisition of steady, limit-cycle data at the frequencies of interest in the experiment with negligible heat loss effects..

A parameterized expression of fuel composition is described in Eq. 1.

$$\chi \left[\eta \left(\frac{3}{2} H_2 + \frac{1}{2} N_2 \right) + (1 - \eta) N H_3 \right] + (1 - \chi) NG \tag{1}$$

The hydrogen fuel used in the experiment is considered to be derived from ammonia as a hydrogen carrier through a decomposition process yielding one part nitrogen to three parts hydrogen. The fraction of hydrogen-nitrogen mixture in the fuel is denoted by χ, where χ=0 corresponds to operation with only natural gas and χ=1 corresponds to operation with no natural gas injected in the fuel stream. The fraction of hydrogen to ammonia is denoted by a decomposition efficiency η. For all test cases reported, the maximum computed χ uncertainty is 2.5%, and the maximum computed η uncertainty is 1.1%. The location of hydrogen injection (premixed with nitrogen) is approximately 70 mm upstream of the burner face to provide some residence time ($\sim$0.5 ms) for premixing while avoiding flashback. This is a common concern with hydrogen due to its high flame speed, low ignition delay time, and high diffusivity.

2.2. Diagnostics

Pressure fluctuations in the combustor were measured using water-cooled, high-frequency piezoresistive transducers (Kulite WCT312M-35/70BARA)

at multiple axial locations in the combustor. The transducers are installed in recessed Helmholtz resonator cavities with a frequency response $> 14\ kHz$ and are sampled at $1MHz$. This installation reduces the thermal load on the sensor element with minimal impact on the accuracy of unsteady pressure measurements within the flow [48, 49]. The locations of the pressure transducers on the combustion chamber are highlighted on the combustor schematic and denoted by the table in Figure 1. Pressure measurements at locations IN, C1, and C2 are aligned along the same azimuthal angle $\theta = 0°$. Additional pressure transducers (GE Sensing UNIK50E6) and k-type thermocouples, sampled at 1 kHz, are located at multiple positions on the combustor and in the fluid infrastructure connected to the experiment. These measurements are used for condition monitoring during the test.

The flame is imaged through a 120 mm long quartz cylinder that provides optical access at the upstream end of the combustion chamber. OH^* chemiluminescence was recorded at 50 kHz in the optical section of the combustion chamber. A UV filter, centered at 320 nm with 40 nm bandwidth (Semrock 320/40 Brightline Bandpass) was used to isolate the signal from background flame luminosity. Flame emission was collected using a 98 mm focal-length, f/2.8 objective lens (Cerco Sodern Type-2178), then amplified by a Lambert HiCATT 25 intensifier with a 1:1 relay lens and recorded with a Phantom v2512 high-speed CMOS camera. OH^* chemiluminescence measurements were obtained with a 15 μs exposure and an image size of 640×432 pixels resulting in a spatial resolution of 0.20 mm/pixel.

3. Results and Discussion

3.1. Parametric Survey of Flame Dynamics

A summary of operating conditions is provided in Table 1. A constant air flow rate of 0.454 kg/s (±0.01 kg/s) was maintained for all tests. The air inlet manifold pressure was maintained at ∼23 bar to ensure a choked inlet to the injector. The air inlet temperature (T_{IN}) was maintained at 762 K (±11 K) for all tests. The combustion chamber pressure of 10.9 bar is maintained with a maximum deviation of 0.7 bar with changes in fuel composition for all cases. Equivalence ratios were selected for a fixed equilibrium flame temperatures (T_{ad}) of 1940 K, consistent with the turbine inlet temperature of combustors with >60% combined cycle efficiency [50, 51]. T_{ad} was maintained within a standard deviation of 60 K. The parameter χ is varied from 50% to 100% in ∼10% increments. Test cases with significant natural gas composition ($\chi \leq 40\%$) resulted in combustion instabilities with consistently high (>10% of p_{CC}) pressure fluctuations and are not presented here. The parameter η is varied from 25% to 100%. A notable decrease in combustion efficiency was observed in test cases with nearly pure ammonia combustion ($\eta < 25\%$) and are not presented here.

Pressure time history for a representative test case is shown in Fig. 2. The test is initiated with laser induced spark ignition of the hydrogen pilot flame that results in a slight increase in chamber pressure at 0 s. Once the pilot flame is established, reactants are introduced through all the injector elements and main flame ignition is achieved at ∼1.4 s. Following main chamber ignition, the hydrogen supply to the pilot injector is disabled. After the reactant flow through all of the injectors reaches the target condition, a

Table 1: Summary of test conditions

Parameter	Value	Units
$\dot{m}_{air}$	0.454	kg/s
p_{IN}	23.0	bar
T_{IN}	762	K
χ	$0.5 - 1.0$	-
η	$0.25 - 1.0$	-
p_{CC}	10.9 ± 0.7	bar
T_{ad}	1940 ± 100	K
ϕ	$0.51 - 0.68$	-

steady p_{CC} of approximately 1.1 MPa is achieved for ∼400 ms. During this period, a transition to limit-cycle dynamics is observed in several test cases. In the limit-cycle regime, the pressure fluctuation amplitude is relatively constant as the amount of energy added into the instability is balanced by loss mechanisms such as viscous dissipation and heat transfer from the chamber walls, and the net energy of the oscillating mode is zero [52]. Pressure and heat release fluctuations are statistically stationary in this regime. A 100 ms sample window from 1.8 s to 1.9 s, where stationary limit-cycle dynamics are consistently observed for all test cases, is used for analysis in the present work. Cessation of pilot hydrogen flow rate was verified in the 100 ms sample window.

The root mean square value of pressure fluctuation (p'_{RMS}) is evaluated from the pressure time history and normalized by chamber pressure for each condition. A map of p'_{RMS}/p_{CC} through systematic variation of χ and η is presented in Figure 3 to illustrate the effects of fuel composition on global flame dynamics. Cases are observed to have relatively low p'_{RMS} amplitudes

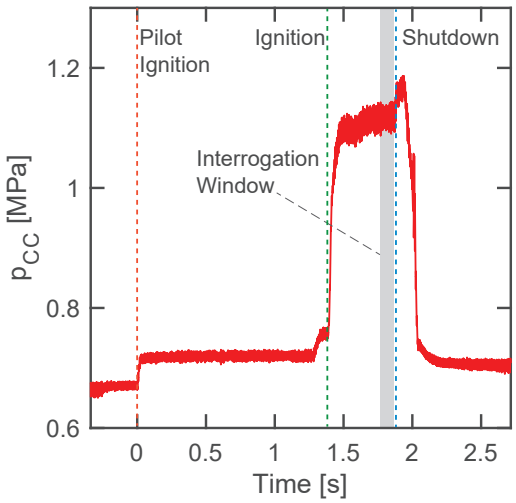

Figure 2: Pressure time history for representative test case with $\chi = 90\%$, $\eta = 100\%$, $T_{IN} = 761$ K, and $\phi = 0.52$.

for large values of χ and η. Decreasing χ results in a monotonic increase in p'_{RMS}/p_{CC}. Decreasing η yields a similar trend, although it is less pronounced for $\chi = 0.9$ and no trend is observed for $\chi = 1.0$. Both χ and η are proportional to hydrogen mole fraction, indicating an increase in instability magnitude as hydrogen is removed from the flame. In hydrogen-natural gas flames ($\eta = 1.00$), low p'_{RMS} magnitudes are observed up to $\chi = 0.7$. Further reduction of hydrogen and replacement with natural gas results in limit-cycle instabilities at p'_{RMS}/p_{CC} magnitudes greater than 5%. For hydrogen-ammonia flames ($\chi = 1.0$), p'_{RMS} is consistently less than 1% of p_{CC} and is largely invariant to ammonia concentration in the fuel. However, a small displacement of hydrogen for natural gas from $\chi = 1.0$ to $\chi = 0.8$ results in p'_{RMS} sensitivity to ammonia concentration, and further reduction of hydrogen through ammonia addition yields p'_{RMS}/p_{CC} magnitudes in excess of 8%.

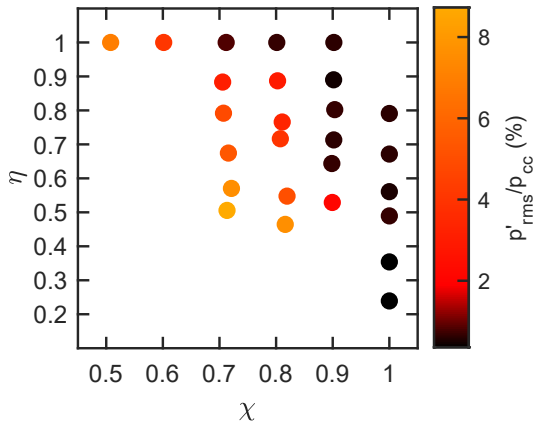

Figure 3: Parametric stability map as a function of hydrogen fraction in fuel χ, and ammonia decomposition efficiency η.

The frequency content of the combustion dynamics observed in the combustor are investigated using discrete Fourier transforms of the pressure signals. Spectral power distribution is plotted for various η at $\chi = 0.7$ to compare the effects of ammonia addition on Figure 4(a).

For cases with no ammonia ($\eta = 1.0$), total p'_{RMS} is low, and a peak is observed at ∼1100 Hz. By decreasing hydrogen through a decrease in η, instability amplitude increases, resulting in a stronger peak near 1100 Hz. Harmonics at ∼2200 Hz and ∼3300 are also observed. The strength of these peaks continues to increase as η decreases to 0.79, and again at 0.67. At $\eta = 0.57$ the combustor transitions to a mode near 550 Hz. This mode persists at $\eta = 0.51$, with a further observed increase in p'_{RMS} indicated by increasing peak intensity in the spectrogram. Harmonics near ∼1100 Hz and ∼1650 Hz are observed when this mode is present. The natural acoustic

frequencies of the system are computed using the Generalized Instability Model [53]. This analysis indicates a fundamental half-wave (1L) longitudinal mode in the combustion chamber at 540 Hz, consistent with the strongest frequency observed at $\eta = 0.57$ and $\eta = 0.51$. The first harmonic of the fundamental frequency is calculated to be 1080 Hz, which denotes a full-wave (2L) mode shape, and is consistent with the ∼1100 Hz frequency observed for $\eta = 0.67 - 1.0$. p'_{RMS} values in test cases where the fundamental mode shape is present are always larger than cases that do not excite this frequency. Slight variations in resonant frequencies are observed with ammonia addition, as seen in the comparison of the $\eta = 0.57$ and $\eta = 0.51$ spectra. These variations can be attributed to minor differences in reactant and product gas composition resulting in non-isotropic acoustic speeds. The changes in convective and reaction timescales can also change the flame heat release and its coupling with chamber acoustics, affecting the frequency and mode-shape of the combustion instability.

Spectral power distribution is also shown in Fig. 4(b) for all $\eta = 1.0$ test cases to compare the effects of natural gas addition. As the concentration of natural gas increases, a growth in instability amplitude is observed with similar trends to those seen in Fig. 4(a). Transition to the fundamental acoustic mode is not present in these cases. Across the operating space, p'_{RMS} is inversely correlated to hydrogen concentration in the fuel, with variations in dominant mode appearing beyond p'_{RMS} thresholds. Understanding of the physical processes that govern the limit-cycle behavior necessitates investigation into the unsteady response of the flame structure, the sensitivity of reaction kinetics to fuel composition, and the effect of these changes on the

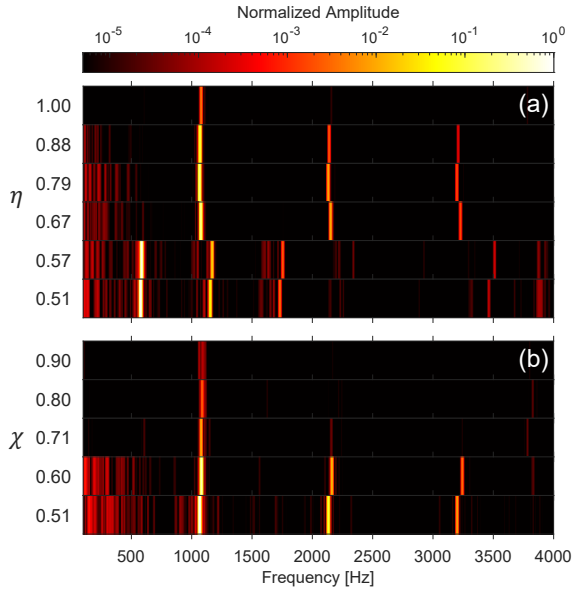

Figure 4: Spectral power distribution of the combustion dynamics for various η at $\chi = 0.7$ (a) and various χ at $\eta = 1.0$ (b) from pressure measurements at location C2.

coupled thermo-acoustic fluctuations.

3.2. Flame Dynamics

Self-excited combustion instabilities are a result of resonant coupling of heat release and pressure fluctuations in the combustor [54]. Therefore, further investigation of the observed combustion dynamics sensitivity to fuel composition requires analysis of the flame response. Instantaneous snapshots of OH^* chemiluminescence measurements for two representative test cases are depicted on Fig. 5. Both cases involve fuel mixtures containing hydrogen and natural gas, with no ammonia present ($\eta = 1.00$). Figure 5(a) contains 60% hydrogen by volume, while Fig. 5(b) contains 71%. This 11% decrease in hydrogen results in distinct OH^* chemiluminescence fluctuations in the upper plot. An increase in flame emission is observed in Fig.5(a) during

the acoustic compression period with increased heat release rates, followed by a large reduction in OH^* concentration during expansion. Conversely, the OH^* emission measured on Fig. 5(b) remains consistent over this period. The frequency of OH^* intensity oscillations is consistent with measured pressure fluctuations shown on Fig. 4(b). The fluctuating component of the OH^* chemiluminescence signal (I') is isolated through mean subtraction of the raw image. Mean OH^* chemiluminescence images ($\bar{I}$) are generated over the 100 ms sampling window for all cases.

Spectral Proper Orthogonal Decomposition (SPOD) is a frequency domain form of proper orthogonal decomposition that yields dynamic modes of statistically stationary flow data [55]. The decomposition of chemiluminescence intensity fluctuations yields energy ranked spatially orthogonal modes corresponding to single frequencies of these fluctuations. The modes are isolated and reconstructed in space and time, which can be used to differentiate flame dynamics between operating conditions. For each condition, intensity fluctuations are decomposed over 50 cycles of the fundamental acoustic mode within the limit-cycle region of the pressure time history. A frequency resolution of 30 Hz is achieved utilizing 8 Hamming window image blocks and 75% window overlap. Additionally, a series of unit root tests are performed on all SPOD data to verify the flame dynamics are statistically stationary [56, 57].

Spatial structure of the I' field for varying η at $\chi = 0.7$ and varying χ at $\eta = 1.0$ are evaluated using SPOD. Phase reconstruction of the spatial mode at the dominant mode frequency is depicted in Fig. 6(a) for cases of increasing ammonia concentration, and for cases of increasing natural gas

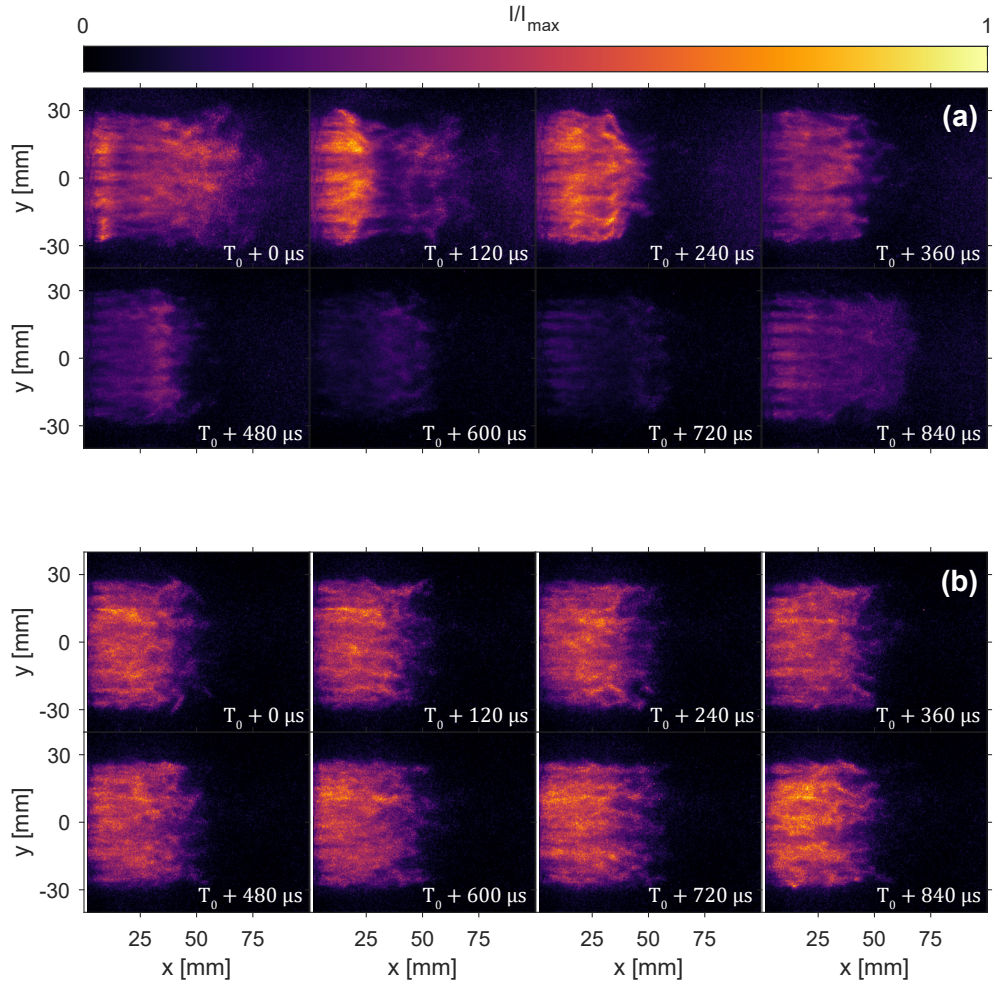

Figure 5: Instantaneous snapshots of OH^* chemiluminescence measurements for $\chi = 0.60$ (a) and $\chi = 0.71$ (b). $\eta = 1.00$ for both cases.

concentration in Fig. 6(b). The reconstructed mode shapes are shown at the phase angle corresponding to a maximum in integrated I' intensity. Spatial reconstruction of the I' distribution provides insight into the extent of heat release at a periodic local maximum that could otherwise be obscured in the mean flame shape. It should be noted that the reconstructed mode shapes

occur at slightly different frequencies. Thus, the images between test cases are consistent in phase, but not time.

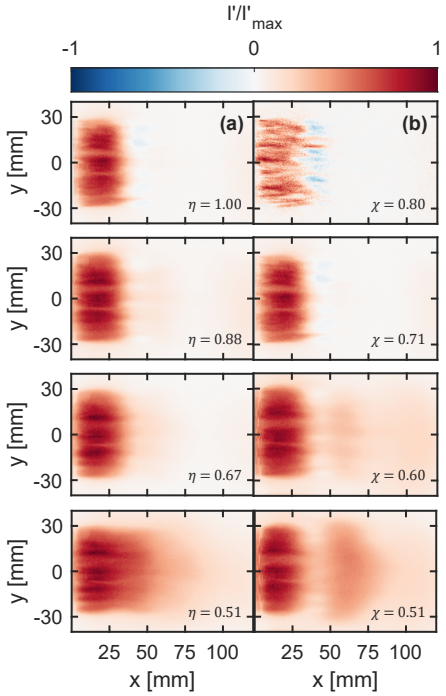

Figure 6: Phase snapshots of dominant SPOD mode reconstruction for ammonia addition (a) and natural gas addition (b).

When a significant fraction of hydrogen is present, the flame response is weak. The spatial structure of the I' signal is compact and localized between x = 0 mm and x = 50 mm. Additionally, flamelets corresponding to individual injector elements are identifiable through slight radial stratification of I'. Radially summed normalized intensity values are shown in Fig. 7 to highlight changes in the length of the oscillating flame with fuel composition. As hydrogen is replaced with ammonia and instability magnitude increases, the axial extent of I' is observed to increase. The heat release fluctuations also appear more uniform radially and are less localized relative

to the injector elements on Fig. 6(a). As η is decreased further and the fundamental 1L mode becomes dominant, a significant lengthening of the flame is observed, with heat release fluctuations extending beyond 50 mm from $\eta = 0.67$ to $\eta = 0.51$. As hydrogen is substituted for ammonia, the expected lengthening of the flame zone is accompanied by stronger acoustic coupling. This correlation remains consistent even through a dominant mode transition, suggesting a requisite distribution of heat release for excitation of the fundamental mode of the combustor to exceed that of its first harmonic (2L mode). Similar trends are observed for replacement of hydrogen with natural gas. Despite the lack of 1L mode excitation in these cases, I' distribution still extends well beyond 60 mm at $\chi = 0.51$ on Fig. 7(b). It is possible that further decrease in χ could lead to excitation of the fundamental mode through continued reductions in flame speed and kinetic timescales.

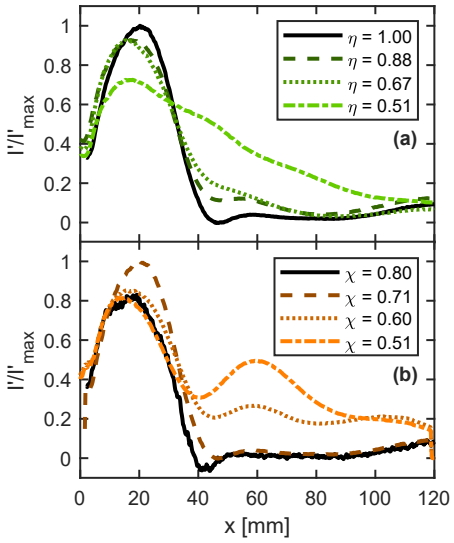

Figure 7: Normalized radial sum of dominant SPOD mode reconstruction at $\psi = 0°$ for ammonia addition (a) and natural gas addition (b).

To further investigate the difference in flame shape with the changing of the dominant acoustic mode, phase snapshots of SPOD mode reconstructions at cases of 1L and 2L mode excitation are illustrated on Fig. 8. While $\chi = 0.7$ for both cases depicted, $\eta = 0.51$ for the fundamental 1L case (Fig. 8(a)) and $\eta = 0.67$ for the first harmonic 2L case (Fig. 8(b)). The reconstructed I' field is computed and plotted at eight phase angles (ψ), ranging from -90° to 225° in 45° increments to compare heat release distributions over an oscillation period. Phase angles $\psi = 0°$ and $\psi = 180°$ are defined as the maximum and minimum integrated I' magnitude, respectively. Both cases are unstable, as indicated by the strong fluctuations observed over the period. The 2L dominant case depicted on Fig. 8(b) shows incipience of positive I' near the burner face at ψ = -90°. Development of this positive region occurs through an increase in I' intensity as the region extends further downstream until it reaches a maximum at $\psi = 0°$. Similar behavior is observed in the appearance, growth, and decay of negative I' intensity from ψ = -90° to $\psi = 225°$. In contrast, the 1L case illustrated on Fig. 8(a) depicts the origin of positive I' ∼50 mm downstream of the burner face. Growth of this positive I' region propagates upstream into the primary flame zone where individual flame elements are observed. Once again, this behavior is observed in the development of negative I' regions as well. Figure 8(a) depicts a flame with a larger ammonia fuel concentration than Fig. 8(b). Ammonia addition decreases chemical reaction rates which leads to unburned reactants persisting farther downstream.

The increased residence of fresh reactants in the combustor leads to more coherent burning and subsequent heat release. This increase is correlated to

excitation of the fundamental acoustic mode of the combustor; a result not observed in unstable cases with more hydrogen.

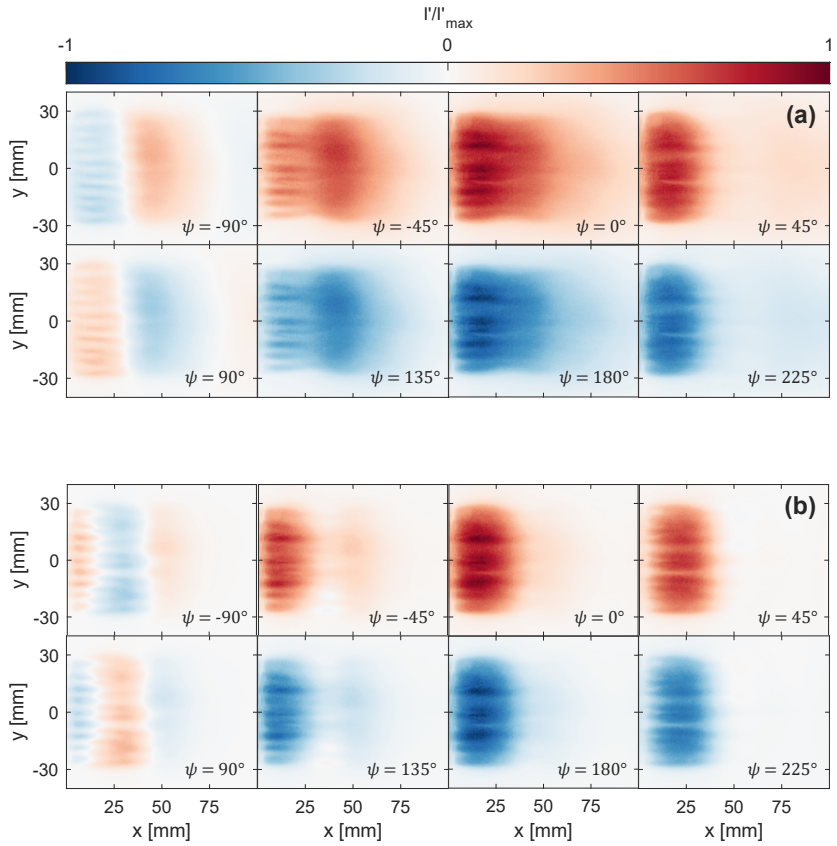

Figure 8: Phase snapshots of dominant SPOD mode reconstruction for fundamental 1L dominant (a) and first harmonic 2L dominant (b) cases. $\chi = 0.7$ for both cases. $\eta = 0.51$ for the 1L case and $\eta = 0.67$ for the 2L case.

3.3. Fuel composition effects on coupled dynamics

The geometry of micromix injectors inherently leads to radially dispersed flamelets. Thus flame shape sensitivity to fuel composition is observed to be predominantly axial, as seen in Fig. 6. This supports the application of one dimensional analysis to characterize fuel composition effects on the cou-

pled interactions between pressure and heat release rate oscillations. Pressure fluctuations in the chamber are decomposed using multivariate singular spectrum analysis (mSSA). Singular spectrum analysis is eigenvalue decomposition technique on a lagged-covariance matrix generated from time series data with a specified window length [58]. The eigenvalues computed from this matrix are empirical orthogonal functions (EOFs) with associated eigenvalue pairs that describe elementary modes of variability. The total variance of the time series is then the sum of the eigenvalues divided by the window length. The EOFs are ranked by eigenvalue importance such that the higher ranked modes have the greatest contribution to the total variance of the signal, and lower ranked modes correspond to stochastic variations. The time series can then be reconstructed with a desired number of the highest ranking modes, which is filtered from the noise. mSSA allows for phase synchronization analysis of a system of coupled oscillators with no prior phase knowledge required [59]. A multivariate system composed of 100 ms time samples of two pressure sensors in the injector, and at least two sensors in the combustion chamber were utilized as the input signal. Each probe is then reconstructed using the fifteen most dominant modes of the system, which accounted for $\sim$93% of the total system variance.

For each reconstructed mode, a one-dimensional (1D) spatial distribution of p' is generated using the computed mode frequency at location C2 and the equilibrium acoustic speed in the chamber determined through chemical equilibrium calculations [60]. A pressure anti-node boundary condition ($dp'/dx = 0$) is enforced at the downstream end of the combustion chamber, which is located at the exit nozzle [53]. The p' amplitude as a function

of axial chamber length is computed using a least-square fit of a sinusoidal wave. The individual 1D profiles are then superposed, yielding a spatial distribution of p' corresponding to the fifteen highest energy modes identified in the mSSA decomposition. An example p' distribution is depicted on Fig. 9. The largest contribution to amplitude is the first harmonic mode (top), which is observed as a full wave in the chamber. Since this mode is a full wave resonator, a resulting pressure anti-node is located at the injector dump plane where the flame stabilizes. Amplitude contributions from the 4L mode are also distinguishable in the combined mode shape. Overall, the combined pressure mode shape shows better agreement with p' measurements at all positions. The coefficient of determination (r^2) is 70% at x/L = 0.26, while r^2 is 21% from the first harmonic mode shape reconstruction.

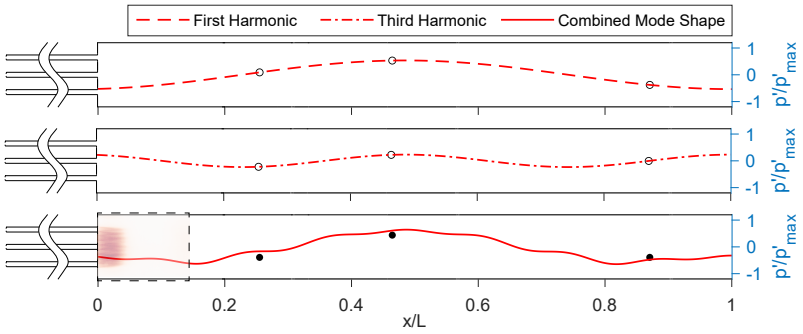

Figure 9: 1-D acoustic reconstruction of the chamber first harmonic mode (top), third harmonic mode (middle), and the fifteen most dominant modes superposed (bottom). Open circles indicated measured p' values filtered at the respective mode, and filled circles are measured p' values unfiltered.

Including chemiluminescence intensity fluctuations in the mSSA decomposition allows for investigation of the phase difference between p' and I' ($\Phi_{p'-I'}$). Combined with the spatial p' distribution, the phase difference be-

tween these fluctuations can be analyzed at the same axial location in the combustor, thus removing phase difference contributions due to convective time delay and spatial mode variations. Time histories are sampled at x/L = 0.02, which corresponds to a location of large I'_{RMS} amplitude for all 1L and 2L dominant cases as depicted in the bottom plot of Fig. 9. For all test cases, $\Phi_{p'-I'}$ is computed for the mode of highest variance identified in mSSA. For unstable cases with strong coherent fluctuations, the identified modes matched those observed in Fig. 4.

Phase differences are plotted in Fig. 10 on the azimuth against p'_{RMS} on the radial axis. Results shown are de-contextualized from the parameterized fuel expression (Eq. 1) to identify trends with respect to fuel mixture properties rather than specific fuel composition. A range of test cases of varying p'_{RMS} magnitudes are observed to have a consistent $\Phi_{p'-I'} \approx \pi/6$. These test cases correspond to unstable cases where the first harmonic mode is most prominent. A separate set of two test cases have an observed $\Phi_{p'-I'} \approx -\pi/6$, which corresponds to test cases where the 1L mode is dominant. A wide range of $\Phi_{p'-I'}$ values is observed in cases where p'_{RMS}/p_{cc} is less than 1%, indicating weak coherence of pressure and heat release fluctuations in these cases.

Table 2: Test conditions of similar $\Phi_{p'-I'}$ depicted in Rayleigh index distribution

Condition	χ	η	p'_{RMS}/p_{cc} [%]	$\Phi_{p'-I'}$ [rad]	$\Phi_{p'-p'}$ [rad]
Low Amplitude (L)	0.90	0.64	0.7	0.61	-0.74
High Amplitude (H)	0.51	1.00	7.0	0.59	-1.15

All unstable cases are observed to have pressure fluctuations and heat

release rate fluctuations between $\Phi_{p'-I'} = -\pi/2$ and $\Phi_{p'-I'} = \pi/2$ at x/L = 0.02. While this is consistent with instability growth per the Rayleigh criterion, there are also low p'_{RMS} test cases depicted that are between $\Phi_{p'-I'} = -\pi/2$ and $\Phi_{p'-I'} = \pi/2$ [61]. To highlight this, representative low amplitude (L) and high amplitude (H) cases are defined in Table 2 and highlighted on Fig. 10. These cases have nearly equivalent $\Phi_{p'-I'} \approx \pi/6$, but differ in p'_{RMS} by an order of magnitude. Therefore, resonant coupling of oscillations in heat release and pressure is necessary for instability growth, but is not a solely sufficient criterion, which is consistent with previous studies. Hong et al. [23] illustrated this through observed mode transitions at $\Phi_{p'-I'}$ values less than the expected result derived from a classical Rayleigh criterion approach. Through a linear acoustic energy balance, they concluded a modified critical $\Phi_{p'-I'}$ that occurs when acoustic energy addition through coupled p' - q' interactions matches acoustic losses at the system boundaries.

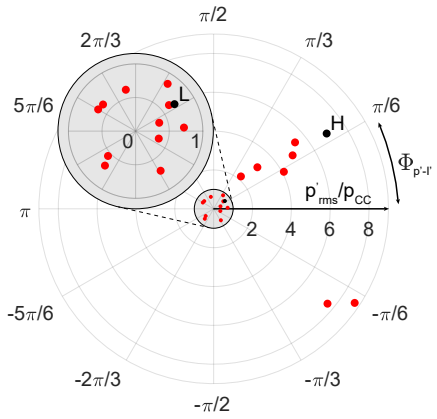

Figure 10: p'-I' phase difference vs p'_{RMS} based on time history data at x/L = 0.02.

Spatial analysis of thermoacoustic coupling in the flame zone is used to il-

lustrate that resonant coupling of heat release and pressure fluctuations alone is not sufficient to drive instability growth. Distributions of the Rayleigh Index (RI) have previously been used in combustion instability experiments to identify regions in the flow-field that lead to instability driving and damping, which is defined by the Rayleigh criterion [39, 54, 62]. Normalized RI distribution maps are calculated with the I' field and the reconstructed p' field using Eq. 2

$$RI = \frac{p' * I'}{p'_{max} * I'_{max}} \tag{2}$$

Instantaneous distribution maps are integrated in time over an acoustic period to capture the total contribution of spatial correlation through an acoustic cycle. Mean cycle integrated RI distribution maps for cases L and H are depicted in Fig. 11.

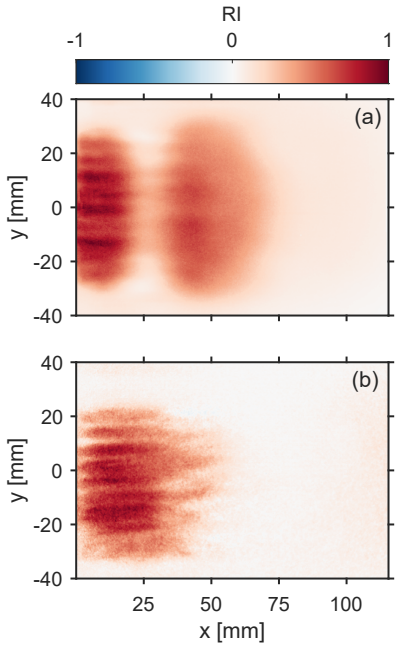

Figure 11: Normalized mean Rayleigh index distribution for Case H (a) and Case L (b)

The high amplitude case depicted in Fig. 11(a) exhibits two distinct regions of positive correlation from x = 0 mm to x = 20 mm, and x = 30 mm to x = 70 mm. The low intensity region from x = 20 mm to x = 30 mm indicates flame pinch off, which acts to increase flame surface area and has been shown to enhance heat release fluctuations [18]. This observed pinch-off could be an indicator of vortex roll-up, a hydrodynamic feature that can develop in unstable flames where the magnitude of bulk fluid oscillations is large [17]. The positively correlated region from 30 mm to 70 mm depicts continuation of coherent burning and heat release downstream of the location of flame pinch-off. A weak intensity gradient from 60 mm to 80 mm designates a reduction in coherence from oscillations in heat release and pressure as residence time in the combustor increases. In contrast to the high amplitude case, a single region of positive correlation is observed in the case depicted on Fig. 11(b) from x = 0 mm to x = 50 mm. Despite positive correlation observed throughout, 11(b) shows weak acoustic coupling with a p'_{RMS}/p_{CC} of less than 1%, suggesting that the resonant coupling in the low amplitude case is not strong enough to overcome the acoustic losses at the boundaries of the combustor. Therefore, sensitivity of $\Phi_{p'-I'}$ to fuel composition is not a sufficient predictor of limit-cycle behavior.

To investigate the role of injector coupling on observed dynamics, mSSA decomposition is performed on pressure sensors at x/L = -0.25 and x/L = 0.25 to determine the phase difference between the injector and combustor. Phase difference between p' measurements at these locations for varying fuel compositions are computed and plotted on the azimuth of Fig. 12 against p'_{RMS} on the radial axis. The computed phase lag between these two p' mea-

surements ($\Phi_{p'-p'}$) is a function of the impedance between the two locations. The two major sources of acoustic impedance between these locations are the injection of hydrogen and the flame. Increased instability magnitude is observed when the total contribution of these sources results in $\Phi_{p'-p'}$ between $-\pi/3$ and $-2\pi/3$. Cases where the 1L mode is dominant and p'_{RMS} magnitude is largest have distinctly larger $\Phi_{p'-p'}$ than cases of 2L dominant dynamics. Additionally, low p'_{RMS} flames are observed for cases where the total impedance between the two locations results in $\Phi_{p'-p'}$ between $-\pi/3$ and $2\pi/3$. Cases L and H specifically differ in $\Phi_{p'-p'}$ by 0.41 radians, highlighting a clear distinction in phase relationship between the combustor and injector that is not present in the analysis of $\Phi_{p'-I'}$ or Rayleigh index distributions. This signifies acoustic coupling between the injector and combustor chamber as a key contributor to instability growth, which is consistent with previous studies [43, 63].

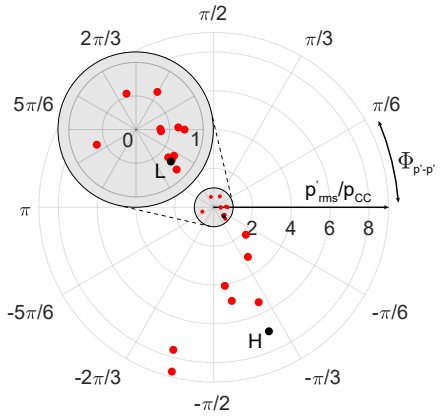

Figure 12: Phase difference between injector and combustor pressure measurements at x/L = -0.24 and x/L = 0.25 respectively vs p'_{RMS}

Further investigation of the contributions from hydrogen injection and the

flame to changes in $\Phi_{p'-p'}$ requires analysis of these two impedance sources independently. To achieve this, the characteristic acoustic impedance is computed for each condition at three locations, prior to hydrogen injection, before the dump plane of the combustor, and in the combustion chamber. Assuming a homogeneous mixture at these locations, the characteristic acoustic impedance is defined as the product of the density and the speed of sound. The ratio of characteristic acoustic impedance from the exit of the injector to the combustion chamber (Z_i/Z_c) is plotted against p'_{RMS} on Fig. 13(a), alongside the impedance ratio across the hydrogen injector (Z_{H0}/Z_{H1}) on Fig. 13(b). No clear correlation is noted between changes in impedance across the flame and changes in limit cycle dynamics. In contrast, a negative correlation between Z_{H0}/Z_{H1} and p'_{RMS} is observed. Although Z_{H0}/Z_{H1} is near unity for all cases, it is unlikely that the total acoustic impedance across this injector is anechoic. Rather, the total acoustic impedance is the sum of the characteristic impedance, and the impedance induced by the blockage from the hydrogen jet. Analysis to quantify the changes to total impedance with hydrogen concentration is nontrivial. A qualitative trend can be discerned however, as increasing H_2 results in farther jet penetration within the micromixer channels. This additional aerodynamic blockage will increase the acoustic impedance across the injector; a trend that is consistent with the observed increase in characteristic impedance. Thus, Z_{H0}/Z_{H1} can be interpreted as a proxy for the total impedance in this instance. The magnitude of this impedance determines the ability for the injector to couple to the dynamics of the combustor. An increase in acoustic impedance across the hydrogen jet trends the remainder of the injector towards a pressure release boundary

condition, thus reducing the capacity of downstream disturbances (ie: pressure fluctuations in the combustion chamber) to propagate upstream. This result is distinctly pertinent to staged, micromix combustors, where additional locations for fuel introduction increase the complexity of the flow-field and smaller premixing elements result in larger impedance contributions from the fuel jets.

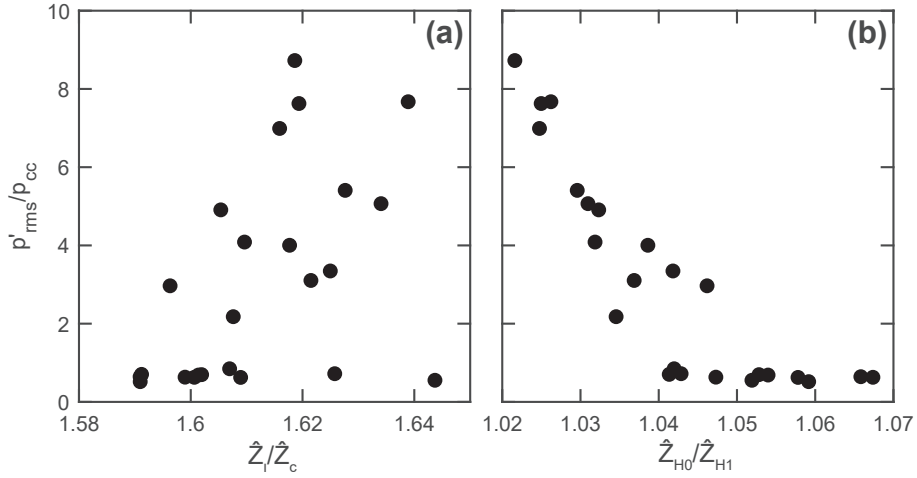

Figure 13: Normalized p'_{RMS} vs ratio of characteristic acoustic impedance across the flame zone (a) and across the micromixer hydrogen injector (b).

3.4. Effect of reactant kinetics

One dimensional, freely propagating premixed laminar flame simulations were performed in Cantera to investigate the effect of chemical kinetics variation through changes in fuel composition on observed flame dynamics [64]. Reactions of air with ammonia, natural gas, hydrogen, and nitrogen are performed using CEU-NH_3-Mech 1.1 [65]. Mechanism selection was based on available validation data at elevated pressures. Experimentally measured inlet conditions were used as model input parameters. The evolution of gas

temperature and heat release rate across the length of the flame is illustrated in Figure 14 for an example test condition at $\chi = 0.51$ and $\eta = 1.0$. For each simulation, the preheat zone begins at the point where the gas temperature rise first exceeds 1% of the total temperature rise. Termination of the preheat zone and start of the flame zone is delineated by a heat release rate increase that first exceeds 1% of the maximum. A flame zone exit boundary is prescribed at the location where the gas temperature reaches 99% of the total temperature rise.

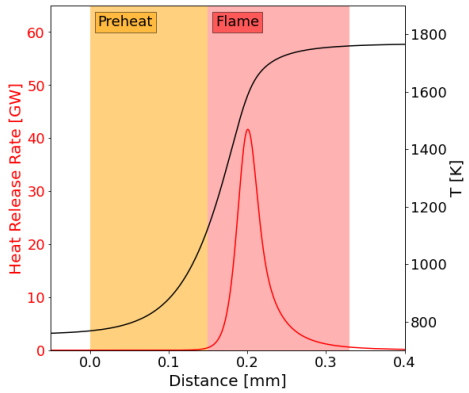

Figure 14: Representative freely propagating premixed laminar flame with preheat and flame regions identified.

Within the freely propagating premixed laminar flame model, the local gas velocity at the start of the preheat zone matches the laminar flame speed. Across the length of the preheat and flame regions, the temperature gradient will result in a decrease in density and acceleration of the flow. At each discrete cell in the model, the time required for the gas to advect through the cell is computed by dividing the cell length by the local velocity. By integrating over the length of the flame, a kinetic timescale (τ_k) is computed. The Damköhler number (Da), defined as the ratio of hydrodynamic timescale

(τ_{flow}) to τ_k, is computed to identify changes in kinetic timescale with fuel composition while accounting for the influence of hydrodynamic sensitivity to the fuel. The hydrodynamic timescale τ_{flow} is computed as $D_{inj}/\bar{U}$, where D_{inj} is the diameter of a single injector element, and $\bar{U}$ is the average injector center-line velocity.

p'_{RMS}/p_{CC} is plotted as a function of Damköhler number on Fig. 15, with test cases of equivalent χ grouped. The largest Damköhler numbers all yield flames with low p'_{RMS} amplitudes. However, both low and high amplitude cases are observed for Da in the range of 0.2 to 0.5. For $\chi = 0.7$ and $\chi = 0.8$, a fairly linear relationship between p'_{RMS}/p_{CC} and Da is observed. Thus, an increase in combustion instability magnitude with ammonia addition can be largely attributed to a decrease in laminar flame speed and an increase in τ_k at these concentrations of natural gas. In contrast, negligible effect on p'_{RMS} magnitude is observed over the range of Damköhler numbers investigated when $\chi = 0.9$ and $\chi = 1.0$. It is possible that further reduction in Damköhler number could lead to larger p'_{RMS} sensitivity at these values of χ, as indicated by the slight increase in p'_{RMS}/p_{CC} at the lowest Da for $\chi = 0.9$. Cases L and H, as seen in Fig. 15, are of similar Damköhler number despite the large disparity in p'_{RMS} magnitude. It has been shown that this disparity is due to changes in acoustic impedance between the combustor and the injector, but it should also be noted that the difference cannot be explained through variations in Damköhler number. While the relationship between kinetic and convective timescales provides indicators for stable combustor operation, analysis of flame kinetics does not sufficiently characterize the influence of fuel composition on the magnitude of limit-cycle dynamics.

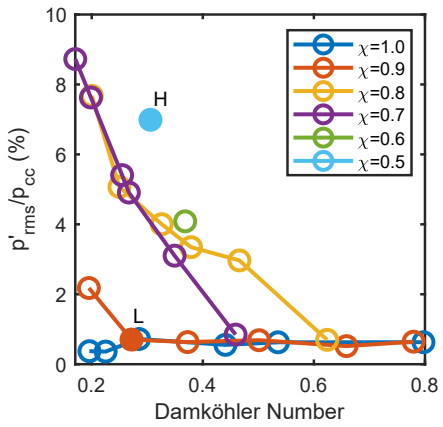

Figure 15: p'_{RMS} vs Damköhler number. Cases of consistent χ grouped.

4. Conclusion

Sensitivity of thermoacoustic combustion instabilities to fuel composition was investigated utilizing fuel blends of ammonia, hydrogen, and natural gas in a combustor operated at 10.9 bar. An axially staged micromix injector was developed with 19 injector elements to uniformly provide premixed reactants to the combustion chamber. Longitudinal instabilities at 550 Hz and 1,100 Hz are observed, corresponding to a half wave and full wave mode of the combustor respectively. As hydrogen concentration was increased, p'_{RMS} magnitude decreased to below 1% of the mean chamber pressure. Cases of largest p'_{RMS} magnitude were consistent with those where the fundamental 1L mode was dominant.

Spatial reconstruction of OH^* chemiluminescence measurements at the dominant mode frequency using SPOD indicate growth in the axial extent of I' intensity as p'_{RMS} increases and hydrogen concentration diminishes. Phase snapshots of SPOD reconstructions were also analyzed at cases of both

1L and 2L mode excitation. When the fundamental 1L mode is dominant a reduction in kinetic rates results in longer residence times for unburned reactants, thereby prompting large coherent heat release fluctuations upon the arrival of the acoustic pressure wave.

Analysis of coupling between fluctuations in pressure and heat release are consistent with the Rayleigh criterion for all unstable cases. However, in-phase coupling between these fluctuations alone is not a sufficient predictor of limit-cycle behavior as the magnitude of the acoustic source must overcome the losses at the system boundaries for instability growth to occur. Phase difference analysis between pressure fluctuations in the injector and the combustor identified an envelope in phase where unstable limit-cycle dynamics occurred. This envelope corresponds to a combined impedance across the hydrogen injector and flame zone that provides sufficient conditions for the injector to couple to the chamber dynamics. Analysis of reaction kinetics shows a linear correlation between limit-cycle p'_{RMS} magnitude and Damköhler number at specific χ values, but does not sufficiently characterize the thermoacoustic dynamics sensitivity to fuel composition over the combustor operating space.

Author contributions

Tristan T. Shahin: Writing – original draft, Writing – review & editing, Investigation, Formal analysis. **Alexander J. Hodge:** Writing – review & editing, Investigation. **Benjamin K. Murdock:** Writing – review & editing, Investigation. **Thomas N. McLean:** Writing – review & editing, Investigation. **Keaton C. Koenig:** Writing – review & editing, Investigation.

Rohan M. Gejji: Writing – review & editing, Supervision, Investigation, Conceptualization. **Robert P. Lucht:** Writing – review & editing, Supervision, Resources, Project administration, Funding acquisition, Conceptualization. **Carson D. Slabaugh:** Writing – review & editing, Supervision, Resources, Funding acquisition, Conceptualization.

Acknowledgements

This work was supported by the Department of Energy University Turbine Systems Research (UTSR) program grant DE-FE0032074 (program manager Andrew O'Connell). The high-speed imaging equipment used in this work was purchased with Defense University Research Instrumentation Program grant FA9550-20-1-0226 (program manager: Chiping Li).

Disclaimer

The views expressed in this article are those of the authors and do not reflect the official policy or position of the United States Air Force, Department of Defense, or the U.S. Government.

References

[1] D. Noble, D. Wu, B. Emerson, S. Sheppard, T. Lieuwen, L. Angello, Assessment of current capabilities and near-term availability of hydrogen-fired gas turbines considering a low-carbon future, Journal of Engineering for Gas Turbines and Power 143 (2021).

[2] H. Kobayashi, A. Hayakawa, K. Somarathne, E. Okafor, Science and technology of ammonia combustion, Proceedings of the Combustion Institute 37 (2019) 109–133.

[3] A. Valera-Medina, F. Amer-Hatem, A. K. Azad, I. C. Dedoussi, M. de Joannon, R. X. Fernandes, P. Glarborg, H. Hashemi, X. He, S. Mashruk, J. McGowan, C. Mounaim-Rouselle, A. Ortiz-Prado, A. Ortiz-Valera, I. Rossetti, B. Shu, M. Yehia, H. Xiao, M. Costa, Review on Ammonia as a Potential Fuel: From Synthesis to Economics, Energy & Fuels 35 (2021) 6964–7029. Publisher: American Chemical Society.

[4] B. Mei, J. Zhang, X. Shi, Z. Xi, Y. Li, Enhancement of ammonia combustion with partial fuel cracking strategy: Laminar flame propagation and kinetic modeling investigation of NH3/H2/N2/air mixtures up to 10 atm, Combustion and Flame 231 (2021) 111472.

[5] S. Sittichompoo, H. Nozari, J. Herreros, N. Serhan, J. Da Silva, A. York, P. Millington, A. Tsolakis, Exhaust energy recovery via catalytic ammonia decomposition to hydrogen for low carbon clean vehicles, Fuel 285 (2021) 119111.

[6] V. Scharl, T. Lackovic, T. Sattelmayer, Characterization of ammonia spray combustion and mixture formation under high-pressure, direct injection conditions, Fuel 333 (2023) 126454.

[7] S. Mashruk, M. O. Vigueras-Zuniga, M. E. Tejeda-del Cueto, H. Xiao, C. Yu, U. Maas, A. Valera-Medina, Combustion features of

CH4/NH3/H2 ternary blends, International Journal of Hydrogen Energy 47 (2022) 30315–30327.

[8] A. A. Khateeb, T. F. Guiberti, G. Wang, W. R. Boyette, M. Younes, A. Jamal, W. L. Roberts, Stability limits and NO emissions of premixed swirl ammonia-air flames enriched with hydrogen or methane at elevated pressures, International Journal of Hydrogen Energy 46 (2021) 11969–11981.

[9] B. Lewis, G. Von Elbe, Stability and Structure of Burner Flames, The Journal of Chemical Physics 11 (1943) 75–97.

[10] A. Kalantari, V. McDonell, Boundary layer flashback of non-swirling premixed flames: Mechanisms, fundamental research, and recent advances, Progress in Energy and Combustion Science 61 (2017) 249–292.

[11] A. Marshall, J. Lundrigan, P. Venkateswaran, J. Seitzman, T. Lieuwen, Measurements of Stretch Statistics at Flame Leading Points for High Hydrogen Content Fuels, Journal of Engineering for Gas Turbines and Power 139 (2017).

[12] J. O'Connor, S. Hemchandra, T. Lieuwen, 7 - combustion instabilities in lean premixed systems, in: D. Dunn-Rankin, P. Therkelsen (Eds.), Lean Combustion (Second Edition), Academic Press, Boston, second edition edition, 2016, pp. 231–259.

[13] T. Lieuwen, H. Torres, C. Johnson, B. T. Zinn, A Mechanism of Combustion Instability in Lean Premixed Gas Turbine Combustors , Journal of Engineering for Gas Turbines and Power 123 (2000) 182–189.

[14] T. Sattelmayer, Influence of the Combustor Aerodynamics on Combustion Instabilities From Equivalence Ratio Fluctuations , Journal of Engineering for Gas Turbines and Power 125 (2002) 11–19.

[15] S. Dhanuka, J. Temme, J. Driscoll, Lean-limit combustion instabilities of a lean premixed prevaporized gas turbine combustor, Proceedings of The Combustion Institute 33 (2011) 2961–2966.

[16] Z. Lim, J. Li, A. S. Morgans, The effect of hydrogen enrichment on the forced response of CH4/H2/Air laminar flames, International Journal of Hydrogen Energy 46 (2021) 23943–23953.

[17] E. Æsøy, T. Indlekofer, M. R. Bothien, J. R. Dawson, The Effect of Hydrogen on Nonlinear Flame Saturation, Journal of Engineering for Gas Turbines and Power 145 (2023) 111019.

[18] H. Kang, M. Lee, K. T. Kim, Measurements of self-excited instabilities and nitrogen oxides emissions in a multi-element lean-premixed hydrogen/methane/air flame ensemble, Proceedings of the Combustion Institute 39 (2023) 4721–4729.

[19] J. Strollo, S. Peluso, J. O'Connor, Effect of Hydrogen on Steady-State and Transient Combustion Instability Characteristics, Journal of Engineering for Gas Turbines and Power 143 (2021) 071023.

[20] J. Beita, M. Talibi, S. Sadasivuni, R. Balachandran, Thermoacoustic Instability Considerations for High Hydrogen Combustion in Lean Premixed Gas Turbine Combustors: A Review, Hydrogen 2 (2021) 33–57. Number: 1 Publisher: Multidisciplinary Digital Publishing Institute.

[21] P. W. Agostinelli, D. Laera, I. Chterev, I. Boxx, L. Gicquel, T. Poinsot, On the impact of h2-enrichment on flame structure and combustion dynamics of a lean partially-premixed turbulent swirling flame, Combustion and Flame 241 (2022).

[22] I. Chterev, I. Boxx, Effect of hydrogen enrichment on the dynamics of a lean technically premixed elevated pressure flame, Combustion and Flame 225 (2021) 149–159.

[23] S. Hong, S. J. Shanbhogue, R. L. Speth, A. F. Ghoniem, On the phase between pressure and heat release fluctuations for propane/hydrogen flames and its role in mode transitions, Combustion and Flame 160 (2013) 2827–2842.

[24] S. Wiseman, A. Gruber, J. R. Dawson, Flame Transfer Functions for Turbulent, Premixed, Ammonia-Hydrogen-Nitrogen-Air Flames, Journal of Engineering for Gas Turbines and Power 145 (2022). 031015.

[25] J. G. Aguilar, E. Æsøy, J. R. Dawson, The influence of hydrogen on the stability of a perfectly premixed combustor, Combustion and Flame 245 (2022) 112323.

[26] A. Valera-Medina, M. Gutesa, H. Xiao, D. Pugh, A. Giles, B. Goktepe, R. Marsh, P. Bowen, Premixed ammonia/hydrogen swirl combustion under rich fuel conditions for gas turbines operation, International Journal of Hydrogen Energy 44 (2019) 8615–8626.

[27] A. Alfazazi, E.-t. Es-sebbar, X. Zhang, B. Dally, M. Abdullah, M. Younes, S. M. Sarathy, Counterflow flame extinction of ammonia

and its blends with hydrogen and C1-C3 hydrocarbons, Applications in Energy and Combustion Science 12 (2022) 100099.

[28] D. E. Thomas, K. P. Shrestha, F. Mauss, W. F. Northrop, Extinction and NO formation of ammonia-hydrogen and air non-premixed counter-flow flames, Proceedings of the Combustion Institute 39 (2023) 1803–1812.

[29] A. M. Elbaz, S. Wang, T. F. Guiberti, W. L. Roberts, Review on the recent advances on ammonia combustion from the fundamentals to the applications, Fuel Communications 10 (2022) 100053.

[30] A. Aniello, T. Poinsot, L. Selle, T. Schuller, Hydrogen substitution of natural-gas in premixed burners and implications for blow-off and flashback limits, International Journal of Hydrogen Energy 47 (2022) 33067–33081.

[31] W. D. York, W. S. Ziminsky, E. Yilmaz, Development and Testing of a Low NOx Hydrogen Combustion System for Heavy-Duty Gas Turbines, Journal of Engineering for Gas Turbines and Power 135 (2013) 022001.

[32] T. Asai, S. Dodo, M. Karishuku, N. Yagi, Y. Akiyama, A. Hayashi, Performance of multiple-injection dry low-nox combustors on hydrogen-rich syngas fuel in an igcc pilot plant, Journal of Engineering for Gas Turbines and Power 137 (2015).

[33] H. Kang, T. Lee, U. Jin, K. T. Kim, Experimental investigation of combustion instabilities of a mesoscale multinozzle array in a lean-premixed

combustor, in: Proceedings of the Combustion Institute, volume 38, Elsevier Ltd, 2021, pp. 6035–6042.

[34] U. Jin, K. T. Kim, Influence of radial fuel staging on combustion instabilities and exhaust emissions from lean-premixed multi-element hydrogen/methane/air flames, Combustion and Flame 242 (2022).

[35] U. Jin, K. T. Kim, Hybrid rich- and lean-premixed ammonia-hydrogen combustion for mitigation of NOx emissions and thermoacoustic instabilities, Combustion and Flame 262 (2024) 113366.

[36] T. Lieuwen, B. T. Zinn, The role of equivalence ratio oscillations in driving combustion instabilities in low NOx gas turbines, Symposium (International) on Combustion 27 (1998) 1809–1816.

[37] M. Stöhr, Z. Yin, W. Meier, Interaction between velocity fluctuations and equivalence ratio fluctuations during thermoacoustic oscillations in a partially premixed swirl combustor, Proceedings of the Combustion Institute 36 (2017) 3907–3915.

[38] S. E. Meyer, S. D. Heister, C. Slabaugh, R. P. Lucht, A. Pratt, R. M. Gejji, M. Bedard, A. Lemcherfi, Design and development of the high pressure combustion laboratory at purdue university, in: 53rd AIAA/SAE/ASEE Joint Propulsion Conference, 2017, p. 4965.

[39] T. Buschhagen, R. Gejji, J. Philo, L. Tran, J. E. P. Bilbao, C. D. Slabaugh, Experimental investigation of self-excited combustion instabilities in a lean, premixed, gas turbine combustor at high pressure, Journal of Engineering for Gas Turbines and Power 140 (2018) 111503.

[40] T. Buschhagen, R. Gejji, J. Philo, L. Tran, J. E. P. Bilbao, C. D. Slabaugh, Self-excited transverse combustion instabilities in a high pressure lean premixed jet flame, Proceedings of the Combustion Institute (2018).

[41] T. Buschhagen, R. M. Gejji, C. Scalo, C. D. Slabaugh, Self-excited instability regimes of a confined turbulent jet flame at elevated pressure, Physics of Fluids 34 (2022) 044103.

[42] R. M. Gejji, T. Buschhagen, C. D. Slabaugh, Occurrence of rotating detonation waves in a jet-stabilized combustor with premixed injection, Journal of Propulsion and Power 0 (2021) 1–5.

[43] J. J. Philo, R. M. Gejji, C. D. Slabaugh, Injector-coupled transverse instabilities in a multi-element premixed combustor, International Journal of Spray and Combustion Dynamics 12 (2020) 1756827720932832.

[44] R. M. Gejji, C. Huang, C. Fugger, C. Yoon, W. Anderson, Parametric investigation of combustion instabilities in a single-element lean direct injection combustor, International Journal of Spray and Combustion Dynamics 11 (2019) 1756827718785851.

[45] American Society of Mechanical Engineers, Measurement of Gas Flow by Means of Critical Flow Venturis and Critical Flow Nozzles, 2016.

[46] International Standards Organization, Measurement of Gas Flow by Means of Critical Flow Venturi Nozzles, 2005.

[47] M. D. Frederick, R. M. Gejji, J. E. Shepherd, C. D. Slabaugh, Time-resolved imaging of the cellular structure of methane and natural gas detonations, Shock Waves (2022).

[48] C. D. Slabaugh, A. C. Pratt, R. P. Lucht, S. E. Meyer, M. Benjamin, K. Lyle, M. Kelsey, The development of an optically accessible, high-power combustion test rig, Review of Scientific Instruments 85 (2014) 035105.

[49] R. M. Gejji, I. V. Walters, S. Beard, A. Lemcherfi, S. V. Sardeshmukh, S. D. Heister, C. D. Slabaugh, Transducer Installation Effects on Pressure Measurements in PGC Devices, 2018.

[50] O. Lammel, H. Schütz, G. Schmitz, R. Lückerath, M. Stöhr, B. Noll, M. Hase, W. Krebs, FLOX Combustion at High Power Density and High Flame Temperatures, Journal of Engineering for Gas Turbines and Power (2010).

[51] M. Yuri, J. Masada, K. Tsukagoshi, E. Ito, S. Hada, Development of 1600°C-Class High-efficiency Gas Turbine for Power Generation Applying J-Type Technology, Technical Report, 2013.

[52] B. T. Zinn, T. C. Lieuwen, Combustion instabilities: basic concepts, Progress in Astronautics and Aeronautics 210 (2005) 3.

[53] J. Portillo, J. Sisco, M. J. Corless, V. Sankaran, W. Anderson, Generalized Combustion Instability Model, in: 42nd AIAA/ASME/SAE/ASEE Joint Propulsion Conference & Exhibit, American Institute of Aeronautics and Astronautics, Sacramento, California, 2006.

[54] W. S. J. B. Rayleigh, The theory of sound. vol. 2, 1896.

[55] A. Towne, O. T. Schmidt, T. Colonius, Spectral proper orthogonal decomposition and its relationship to dynamic mode decomposition and resolvent analysis, Journal of Fluid Mechanics 847 (2018) 821–867.

[56] D. A. Dickey, W. A. Fuller, Likelihood Ratio Statistics for Autoregressive Time Series with a Unit Root, Econometrica 49 (1981) 1057–1072. Publisher: [Wiley, Econometric Society].

[57] D. Kwiatkowski, P. C. B. Phillips, P. Schmidt, Y. Shin, Testing the null hypothesis of stationarity against the alternative of a unit root: How sure are we that economic time series have a unit root?, Journal of Econometrics 54 (1992) 159–178.

[58] R. Vautard, P. Yiou, M. Ghil, Singular-spectrum analysis: A toolkit for short, noisy chaotic signals, Physica D: Nonlinear Phenomena 58 (1992) 95–126.

[59] A. Groth, M. Ghil, Multivariate singular spectrum analysis and the road to phase synchronization, Phys. Rev. E 84 (2011) 036206.

[60] S. Gordon, B. J. McBride, Computer Program for Calculation of Complex Chemical Equilibrium Compositions and Applications II. Users Manual and Program Description, Technical Report NASA-RP-1311, NASA Lewis Research Center, Cleveland, OH, United States, 1996.

[61] T. Schuller, T. Poinsot, S. Candel, Dynamics and control of premixed combustion systems based on flame transfer and describing functions, Journal of Fluid Mechanics 894 (2020) P1.

[62] P. Kasthuri, S. A. Pawar, R. Gejji, W. Anderson, R. I. Sujith, Coupled interaction between acoustics and unsteady flame dynamics during the transition to thermoacoustic instability in a multi-element rocket combustor, Combustion and Flame 240 (2022) 112047.

[63] S. Gröning, J. S. Hardi, D. Suslov, M. Oschwald, Injector-Driven Combustion Instabilities in a Hydrogen/Oxygen Rocket Combustor, Journal of Propulsion and Power 32 (2016) 560–573. Publisher: American Institute of Aeronautics and Astronautics _eprint: https://doi.org/10.2514/1.B35768.

[64] D. G. Goodwin, R. L. Speth, H. K. Moffat, B. W. Weber, Cantera: An object-oriented software toolkit for chemical kinetics, thermodynamics, and transport processes, 2021. Version 2.4.0.

[65] S. Wang, Z. Wang, C. Chen, A. M. Elbaz, Z. Sun, W. L. Roberts, Applying heat flux method to laminar burning velocity measurements of nh3/ch4/air at elevated pressures and kinetic modeling study, Combustion and Flame 236 (2022).

Appendix A. Summary of All Test Conditions

A detailed summary of all test conditions presented in this work is provided in Table A.3.

Table A.3: Summary of all test conditions.

Condition	$\dot{m}_{air}$ [kg/s]	p_{IN} [bar]	T_{IN} [K]	p_{CC} [bar]	T_{ad} [K]	χ	η	ϕ	p'_{rms}/p_{CC} [%]
1	0.452	22.8	758	11.2	1904	1.00	0.79	0.53	0.63
2	0.464	23.4	758	11.5	1899	1.00	0.67	0.54	0.63
3	0.457	23.0	758	11.4	1972	1.00	0.57	0.60	0.43
4	0.457	23.0	757	11.6	1953	1.00	0.56	0.58	0.55
5	0.449	22.6	760	11.0	1909	1.00	0.49	0.56	0.72
6	0.450	22.6	759	11.2	1973	1.00	0.35	0.62	0.36
7	0.450	22.6	759	11.5	2039	1.00	0.24	0.68	0.37
8	0.459	23.2	762	11.1	1901	0.90	1.00	0.52	0.64
9	0.462	23.4	773	11.1	1912	0.90	0.89	0.53	0.52
10	0.454	23.0	764	10.6	1906	0.90	0.80	0.53	0.69
11	0.452	22.9	765	10.5	1888	0.90	0.71	0.53	0.63
12	0.448	22.7	765	10.3	1858	0.90	0.64	0.51	0.70
13	0.449	22.6	755	10.6	1848	0.90	0.53	0.52	2.18
14	0.453	23.0	770	11.0	1923	0.80	1.00	0.54	0.70
15	0.463	23.5	772	10.9	1901	0.80	0.89	0.53	2.97
16	0.449	22.6	758	10.4	1920	0.81	0.77	0.55	3.35
17	0.458	23.2	762	10.5	1908	0.81	0.72	0.54	4.00
18	0.452	22.9	761	10.5	1919	0.82	0.55	0.56	5.07
19	0.448	22.6	759	10.4	1912	0.82	0.46	0.56	7.67
20	0.463	23.4	762	11.0	1895	0.71	1.00	0.53	0.85
21	0.456	22.9	751	10.7	1886	0.71	0.88	0.53	3.10
22	0.462	23.3	760	10.6	1864	0.71	0.79	0.52	4.91
23	0.451	22.7	760	10.3	1906	0.72	0.67	0.55	5.41
24	0.460	23.3	764	10.4	1888	0.72	0.57	0.54	7.63
25	0.454	23.0	764	10.2	1878	0.71	0.51	0.53	8.73
26	0.454	23.0	768	10.6	1901	0.60	1.00	0.53	4.09
27	0.455	23.0	764	10.4	1892	0.51	1.00	0.53	6.99